

# Genetic algorithm driven optimization of a guided mode resonator coupled to an infrared nanocrystal film

Cite as: Appl. Phys. Lett. **125**, 171108 (2024); doi: [10.1063/5.0227684](https://doi.org/10.1063/5.0227684)

Submitted: 10 July 2024 · Accepted: 13 October 2024 ·

Published Online: 24 October 2024



Claire Abadie,<sup>1</sup> Nicolas Ledos,<sup>1</sup> Ye Mou,<sup>1</sup> Mariarosa Cavallo,<sup>1</sup> Erwan Bossavit,<sup>1</sup> Huichen Zhang,<sup>1</sup> Albin Colle,<sup>1</sup> Tommaso Gemo,<sup>1</sup> Adrien Khalili,<sup>1</sup> Yoann Prado,<sup>1</sup> Bruno Gallas,<sup>1</sup> Gregory Vincent,<sup>2</sup> Mathieu Mivelle,<sup>1</sup> and Emmanuel Lhuillier<sup>1,a)</sup>

## AFFILIATIONS

<sup>1</sup>Sorbonne Université, CNRS, Institut des NanoSciences de Paris, 4 place Jussieu, 75005 Paris, France

<sup>2</sup>DOTA, ONERA, Université Paris Saclay, 6 Chemin de la Vauve aux Granges, 91120 Palaiseau, France

**Note:** This paper is part of the APL Special Collection on Mid and Long Wavelength Infrared Photonics, Materials, and Devices.

<sup>a)</sup>Author to whom correspondence should be addressed: [el@insp.upmc.fr](mailto:el@insp.upmc.fr)

## ABSTRACT

Nanocrystal (NC)-based devices suffer from a trade-off between absorption, pushing for thicker films, and charge conduction that is only efficient over a few NC sizes. Therefore, the design of detectors based on NCs strongly benefits from the introduction of optical resonators that engineer the light-matter coupling. Traditionally, the design of such a cavity relies on analytic scaling rules. However, the design becomes far more complex when multiple resonances are targeted, requiring alternative design strategies. In this study, we explore how infrared nanocrystals can be coupled to a guided mode resonator to achieve a broadband enhancement of absorption. A genetic algorithm is used to systematically investigate how geometric factors can be tuned to increase the absorption  $\times$  bandwidth product. In comparison to the pristine film, a significant increase in absorption was demonstrated across the targeted spectral range (1–2.5  $\mu\text{m}$ ). The detector based on the design metasurface exhibited high detectivity ( $2 \times 10^{10}$  Jones @ 200 K) and fast time response (18 ns).

Published under an exclusive license by AIP Publishing. <https://doi.org/10.1063/5.0227684>

Nanocrystals (NCs) provide a unique platform for optoelectronics by combining broad spectral tunability with charge conduction, enabling electrical addressing of their optical features. However, their polycrystalline nature leads to a hopping conduction process, which is often viewed as a limitation due to moderate carrier mobility and charge diffusion length.<sup>1</sup> This leads to a trade-off when the film is used as an active layer for light sensing. Charge collection is only efficient over a short distance, typically a few NC, while their absorption depth exceeds 1  $\mu\text{m}$ . This results in an overall poor coupling of the light with the NC film, leading to weak absorption for detectors and limited coupling to the far field for light-emitting devices.

To avoid such bottlenecks, the field has been very active in coupling the NC layer with a photonic structure. This ensures that the light-matter interaction is not solely driven by the material itself. Various photonic designs have been tested,<sup>2</sup> including plasmonic metallic structures,<sup>3,4</sup> Fabry-Perot cavities,<sup>5</sup> either at macroscopic scale or subwavelength scale using metal insulator metal cavities<sup>6–8</sup> and dielectric counterparts based on Bragg mirrors,<sup>9–11</sup> nanoantennas,<sup>12,13</sup>

bound states in the continuum resonance,<sup>14,15</sup> and more exotic concepts<sup>16,17</sup> inspired by acoustic or millimeter waves. Thanks to the local Kirchhoff's law,<sup>18,19</sup> which states that emission is proportional to absorption at the same wavelength, this concept can be used to shape either the absorption or emission signal. Significant performance enhancement has been made by coupling the NC layer to a photonic cavity,<sup>6</sup> resulting in increased absorption and photoluminescence signals,<sup>11,20</sup> spectral shaping, directivity of light emission,<sup>9,11,21</sup> and the design of active devices<sup>1,4,22</sup> with spectra that can be reversibly reconfigured through the application of a bias.

This approach aims to maximize the modulus of the electric field within the NC layer (excluding the contact that does not generate photocurrent or photoluminescence) by utilizing the cavity design. In practice, and for the case of a single resonance, geometrical factors of the cavity are tuned to match its resonance wavelength to the NC cut-off wavelength.

Further scaling of the cavity factor will then depend on the targeted application. For instance, luminescence, lasing, and gas sensing

spectroscopy benefit from strategies based on a high-quality factor cavity, resulting in spectrally narrow features. Conversely, imaging is a broadband application that requires an increase in the system gain  $\times$  bandwidth product. Therefore, the electric field modulus should be enhanced over a broad spectral range, which may require combining several resonances. Several examples have already been reported of combining two types of cavities<sup>23</sup> (Fabry–Perot and Plasmon) or using a multiresonant cavity.<sup>24,25</sup> However, the idea of combining multiple cavities to achieve several resonances quickly encounters fabrication challenges. In solar cells, Chen *et al.*<sup>26</sup> propose aggregating up to nine resonances to cover the entire visible range. Although the device achieves strong broadband absorption, the challenges raised by fabrication strongly balance the benefit of the concept. Conversely, a broadening of the linewidth may also be obtained by stacking diodes with various band edges similar to multi-junction solar cells. This however also leads to a more complex device design and may expose the NCs to damaging fabrication steps (annealing<sup>27</sup>). Using a polydisperse NC film is also likely to broaden the band edge. However, this approach will come at the cost of increased dark current, as it is driven by the narrowest bandgap material.

Therefore, alternative design strategies are necessary for the development of such a broadband detector. Here, we adopt a resonator design strategy based on a genetic algorithm that does not make assumptions about the nature of the injected mode, other than the fabrication constraints that are initially set. Thanks to this approach, we are able to design a structure that maximizes the product of the absorption magnitude by its bandwidth. The nature of the various resonance is then discussed and we finally quantify the performances of a detector based on such resonator.

In this study, our interest had been focused on extended short-wave infrared (SWIR) NCs, with a  $2.5\text{ }\mu\text{m}$  cutoff wavelength. Compared to traditional InGaAs alloy active in the SWIR, the NCs lift the constraint of the epitaxial growth, which eases the spectral tunability (i.e., no need to be lattice matched with the substrate) and simplifies the coupling to a readout circuit as in the case of cameras.

This publication focuses on guided mode resonator<sup>28</sup> (GMR) geometry, specifically a type of resonator that uses a grating to transform the incident plane wave of light into a propagative mode along the substrate. This approach enables multiple passes of the incident light into the absorbing layer, resulting in increased absorption. The concept has already been applied to nanocrystal-based devices with photoconductive,<sup>29</sup> phototransistor,<sup>30</sup> and photovoltaic<sup>31</sup> configurations. This highlights the method's effectiveness in generating devices that absorb most of the incident light.

A way to generate such GMR relies on the structure schematized in Fig. 1(a). A back side mirror is first deposited onto a substrate and coated with a silica spacer. Then a metallic grating is fabricated on top of the silica layer. In its classical form the grating is periodic.<sup>29–31</sup> It can also serve as interdigitated electrodes, providing a dual role in both enhancing the electromagnetic field and collecting charges. With a periodic structure, the period ( $p$ ) sets the resonance wavelength ( $\lambda_r$ ) based on the equation  $p = \lambda_r/n$ , where  $n$  is the refractive index of the active material. For HgTe NCs with a  $2.5\text{ }\mu\text{m}$  cutoff wavelength, the value of  $n$  has been determined to be around 2.3 through ellipsometry.<sup>31</sup> The extinction loss was estimated to be around 0.1 at the exciton, see Fig. S1 and the associated section for the dielectric parameter of each layer.

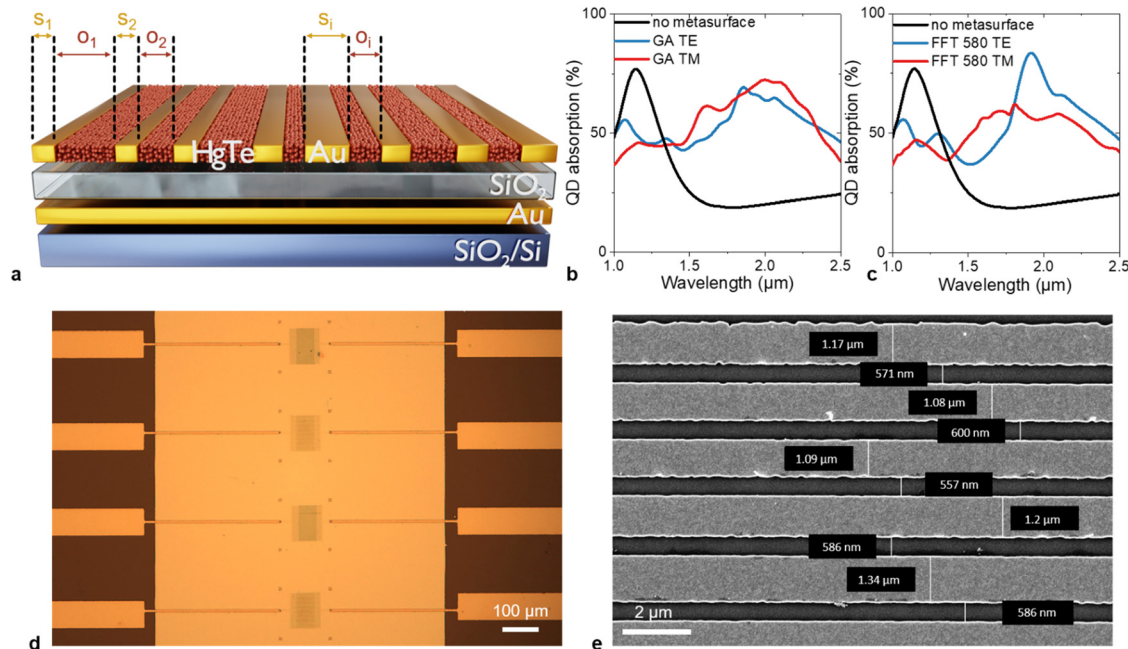


**FIG. 1.** Guided mode resonator coupled to an infrared NC film. (a) Schematic of the guided mode resonator under optimization through a genetic algorithm. (b) Simulated absorption spectra for the pristine NC film and for the film coupled to the optimized GA structure. (c) Simulated absorption spectra for the pristine NC film and for the film coupled to the optimized GA structure after an FFT filtering and setting all values for  $O_1 = 580\text{ nm}$ . (d) Optical microscopy image of the structure (GMR GA FFT580) before NC film deposition. (e) Scanning electron microscopy image of the structure (GMR GA FFT580) before NC film deposition.

A genetic algorithm (GA) optimization is then initiated for this structure, subject to the following constraints: the thickness of the gold backside mirror is set to 80 nm, a value above the metal skin depth, and the bottom spacer is made of 120 nm of SiO<sub>2</sub> to prevent a short circuit between the bottom gold mirror and the top grating. The grating consists of 5 nm of Ti (later modeled as an additional 5 nm of gold) and 80 nm of gold. These values were directly taken from previous works on GMR coupled to NC films.<sup>32</sup> However, the size of the digit ( $S_i$ ) and the opening size between digit ( $O_i$ ), see Fig. 1(a), are set as free parameters. We initially set a minimum value for  $O_i$  above >200 nm to prevent shorts during the e-beam process. The size of the grating array is set to 100  $\mu\text{m}$  to avoid stitching issues, which can be patterned from a single field of view in most standard scanning electron microscopes. The deposition conditions of the NC layer are optimized, including concentration and deposition speed, to achieve a thickness as close as possible to 300 nm.

Each structure is represented by a 1-by- $n$  vector, where  $n \leq 250$ , that describes all values for  $O_i$  and  $S_i$  parameters. The generation size is set at 400, with each generation comprising 200 unique structures. In each subsequent generation, 100 structures are generated through mutation [i.e., one or more  $O_i/S_i$  parameters are randomly replaced with new value(s)], while the remaining 100 are produced through breeding (i.e., merging a series of  $S_i/O_i$  parameters to form a new structure). Mutation occurs at a rate of 10%, meaning that  $0.1 \times n$  elements within a structure are randomly altered. Breeding is performed through two-point scattering breeding, where two elements from two structures are randomly selected and exchanged between the structures.

Then for each structure, we evaluate the absorption spectra relative to the structure using FDTD software (Lumerical). This absorption map is then spatially integrated over the volume of the NC film ( $V_{\text{NC}}$ ) only (i.e., excluding the contact that does not generate photocurrent, but only thermal heat),

$$Abs_{\text{NC}}(\omega) = \frac{P_{\text{NC}}(\omega)}{P_{\text{incidence}}} = \frac{\iiint 0.5\omega |F|^2 \epsilon_0 \text{Im}(\epsilon) dV_{\text{NC}}}{P_{\text{incidence}}}. \quad (1)$$

We then extract from the absorption spectra the parameter  $S$ , which is the integral of the absorption from 1 to 2.5  $\mu\text{m}$ . The 1  $\mu\text{m}$  limit is set to focus on the infrared spectral response, while the value of 2.5  $\mu\text{m}$  matches the NC cutoff.

$$S = \int_{1\mu\text{m}}^{2.5\mu\text{m}} Abs_{\text{NC}}(\omega). \quad (2)$$

Finally, the  $S$  value is normalized by the value obtained for the same stack without the gold stripes (i.e., the NC layer with the same thickness deposited on the gold backside mirror on top of the silica spacer). Figure 1(b) displays the absorption spectra obtained for the reference (i.e., without nanostructure) and for the GA-optimized structure. Even without patterning, the absorption displays a clear resonance, that we can attribute to a vertical Fabry-Pérot (see Fig. S2). However, the resonance appearing at 1.2  $\mu\text{m}$  does not match the band edge. The linewidth of this resonance is typically around 300 nm.

The performance of a given structure is evaluated using the normalized  $S$  parameter as a figure of merit. The optimal structure was identified in the 384<sup>th</sup> generation, as shown in Fig. S3. The associated absorption spectra can be found in Fig. 1(b). The resonance compared

to the pristine film is shifted toward longer wavelengths (i.e., closer to the band edge) and clearly broadened compared to a periodic structure (Fig. S4). The magnification of the absorption occurs over 1500 nm, stressing the benefit of this approach compared to the single resonance method resulting from Fabry-Pérot, for which enhancement occurs only over 300 nm. Additionally, several sub-features are visible, indicating that multiple resonances are involved, contributing to a significant broadening of the overall absorption enhancement. The absorption maps, at the point of maximum absorption, are displayed in Fig. S5. The modes remain close to the expected mode for the periodic structure, although we observe modulations of the field intensity depending on the exact localization within the structure.

Then, the structure was fabricated following the procedure outlined in Fig. S8. After fabrication, the metasurface was coated with HgTe NCs presenting a band edge at around 2.5  $\mu\text{m}$  and grown using the Keuleyan's procedure.<sup>33</sup> However, a limited number of devices were viable due to the presence of shorts. The difficulty comes from the optimization of the electron dose for the lithography procedure. The random organization of large and small openings resulting from the GA method makes this dose optimization challenging. Thus, we set an additional degree of constraint by setting all the openings equal to  $O_i = 580$  nm, which corresponds to the average value over the entire structure obtained after the GA procedure. The choice of this value appears noncritical since a 20 nm change in this value barely impacts the absorption spectra (Fig. S6). We further truncate the FFT distribution to a given threshold ( $0.25 \mu\text{m}^{-1}$ ), which results in the structure becoming periodic with a super-period that includes seven digits. The simulated spectra are shown in Fig. 1(c). The next structure, called GMR GA FFT 580, was imaged using optical and electron microscopy as shown in Figs. 1(d) and 1(e), respectively.

The benefits of the metasurface are evident from the absorption measurements taken over and away from the grating using infrared microscopy, as depicted in Fig. 2(a). The first expected result is a clear

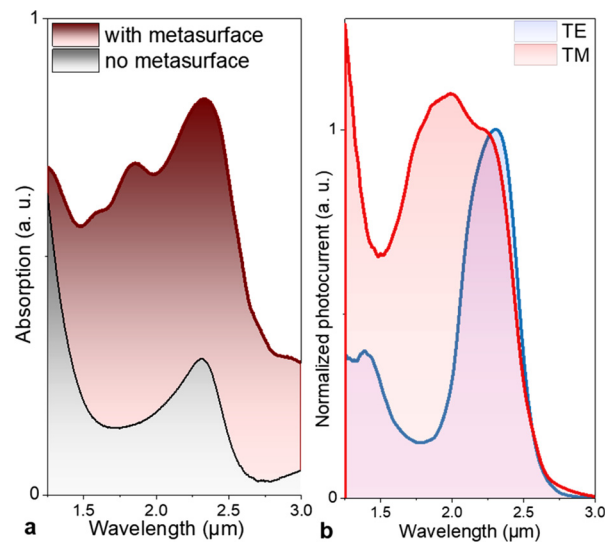


**FIG. 2.** Spectra from the GMR GA FFT580. (a) Absorption spectrum from the GMR GA FFT580 coupled to HgTe NC film. (b) Photocurrent spectra from the GMR GA FFT580 coupled to HgTe NC film in TM and TE polarization.

TABLE I. Strategies for multiresonant infrared detector based on HgTe NCs.

Number of resonances involved	Nature of the resonances	Maximum absorption	Linewidth of the resonance	References
3	Plasmon+vertical Fabry-Perot+planar Fabry-Perot	60%	1200 cm <sup>-1</sup>	6 and 34
3	Plasmon+vertical Fabry-Perot+planar Fabry-Perot	55%	2000 cm <sup>-1</sup>	22 and 24
2	Double Fabry-Perot	25% at band edge + 50% on second	≈800 cm <sup>-1</sup>	35
2	Plasmon+vertical Fabry-Perot	80%	500 cm <sup>-1</sup> @2250 cm <sup>-1</sup> + second peak @5800 cm <sup>-1</sup>	23
4 main	GMR+Fabry-Perot+high order mode	80%	3000 cm <sup>-1</sup>	This work

rise of the absorption magnitude, not only at the band edge but also away from it. Additionally, the absorption is enhanced for wavelengths beyond the band edge, which we attribute to the extra metallic losses resulting from the increased amount of metal within the metasurface. In the photocurrent spectra [Fig. 2(b)], we recover the different features seen in absorption and find that the band edge mostly matches with the TE polarization, which dominates in terms of amplitude. Meanwhile, the TM polarization strongly contributes to broaden the overall signal at higher energy. Table I makes a comparison of various strategies of design for multiresonant photonic structure coupled to HgTe NC film and shows that the current strategies are indeed well suited to generate a broad absorption enhancement.

The GA procedure leaves the exact nature of the involved electromagnetic modes unclear, requiring further investigation. Dispersion maps [Figs. 3(a) and 3(b)] provide initial insight in this direction. Around the NC band edge (2.3 μm peak), the dispersion in TE

polarization clearly shows a strongly dispersive mode that splits into two branches under oblique incidence. Its absorption is both located on top of the digit of the grating and in the opening between digits, but very weakly localized in the metal, see Fig. 3(c). This mode matches the expected behavior for a GMR. The absorption in the TM polarization close to the band edge is dominated by a non-dispersive mode, in which absorption is mostly localized on top of the metal digit.

Figure S7 shows a change in the magnitude of the absorption spectrum with thickness but no shift, while the resonance condition for a vertical Fabry-Perot cavity is that the thickness is a multiple of λ/n with λ being the resonance wavelength and n the refractive index. Thus, we should look for other possible resonances and, in particular, for the formation of a horizontal Fabry-Pérot cavity.<sup>24</sup> The latter results from the discontinuity of the effective index for the NC film on top of the dielectric and on top of the metal digit. Although this combination of GMR and cavity mode are similar to the mode that can be generated

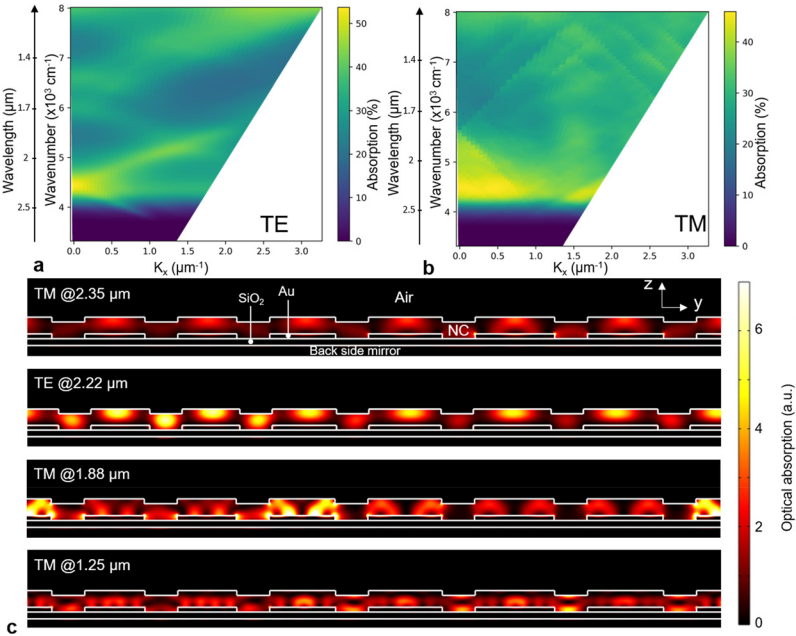
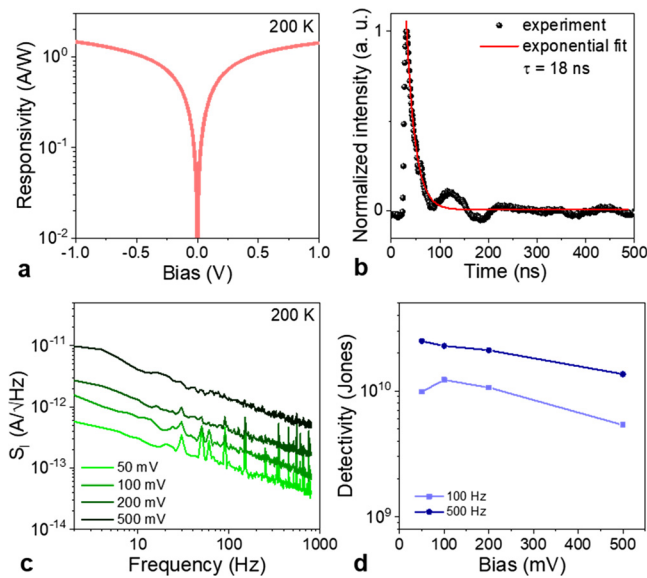


FIG. 3. Optical mode determination from the GMR GA FFT580 coupled to HgTe NC film. (a) [resp (b).] Dispersion map in TE (resp TM) polarization for the GMR GA FFT580 structure. (c) Simulated absorption map at various wavelengths and polarizations corresponding to resonance in the absorption spectra [Fig. 2(a)].





**FIG. 4.** Detection properties from the GMR GA FFT580. (a) Responsivity as a function of the applied bias, measured at 200 K. (b) Time response after a 1 ns pulse at  $1.57 \mu\text{m}$  (bias = 0.2 V). (c) Current spectral density as a function of the signal frequency while various biases are applied over the device. (d) Specific detectivity as a function of the applied bias for two signal frequencies at 200 K.

from a periodic grating design<sup>24</sup> (Fig. S9) close to the band edge, a key difference with the single period design is the presence of extra resonances at high energy. For the sake of illustration, absorption maps at  $1.25$  and  $1.88 \mu\text{m}$  are also shown in Fig. 3(c). These modes appear more complex (i.e., non-repetitive over the whole pattern) over to analyze since they appear more localized (TM at  $1.88 \mu\text{m}$ ) or resulting from a high-order mode as the absorption map depicts several nodes (TM at  $1.25 \mu\text{m}$ ). Those extra modes are responsible for the broad absorption enhancement generated by the GA method.

The device's responsivity exceeds  $1 \text{ A W}^{-1}$  when operated with a bias of 1 V and at a temperature of 200 K [Fig. 4(a)]. This corresponds to an external quantum efficiency of  $\approx 50\%$ , since the absorption around the band edge averages at 70%, the internal quantum efficiency is also around 70%. Noise in the system has been measured to be  $1/f$  limited [Fig. 4(c)], which is the usual behavior for a photoconductive device based on narrow bandgap NCs. The resulting specific detectivity (in Jones) of the sample is determined using the formula:  $D^* = \frac{R\sqrt{A}}{S_i}$ , where  $R$  (in  $\text{A W}^{-1}$ ) is the responsivity,  $S_i$  is the noise ( $\text{A}/\sqrt{\text{Hz}}$ ), and  $A$  is the area of the device taken in square centimeters (in this case  $100 \times 50 \mu\text{m}^2$ ). Values above  $2 \times 10^{10}$  Jones, under 0.1 V, have been achieved, see Fig. 4(d). This value is one order of magnitude lower than the values currently achieved for this material when integrated into a vertical geometry photodiode.<sup>36–39</sup> Since the responsivity values are similar between the diode and our film coupled to the GA-optimized resonator, the main difference arises from the noise magnitude, resulting from the higher bias operation of our photoconductor. Certainly, future efforts should focus on transferring this concept of GA-optimized resonator into a diode device. However, the reduced signal-to-noise ratio is balanced by a higher temporal bandwidth. The time response of the sensor appears very fast with an exponential decay

fit determined to be 18 ns [Fig. 4(b)]. This value is 10 times faster than that reported for a vertical geometry device operating in the short-wave infrared and based on the same materials.<sup>36–38</sup>

To summarize, we have investigated how the combination of multiple resonances shapes the spectral response of a photoconductive device in a way that increases the gain  $\times$  bandwidth product. However, this combination becomes complex when analytic scaling rules are lost or due to increasing fabrication complexity. Therefore, a complementary method based on a genetic algorithm optimization is pursued. The absorption resulting from the metasurface-coupled film is increased in both magnitude and linewidth compared to the uncoupled pristine film. Our findings indicate that the mode near the semiconductor band edge remains similar to the one obtained for a periodic structure, but additional modes at high energy are present, being either localized or resulting from high-order modes. We demonstrate that such an advanced design for the resonator enables a clear enhancement of the absorption  $\times$  bandwidth product.

See the [supplementary material](#) for details on (i) nanocrystal growth, (ii) input for electromagnetic simulation, (iii) structure optimized through genetic algorithm, (iv) device fabrication and characterization, and (v) simulation for periodic structure.

The project is supported by ERC grant AQDtive (Grant No. 101086358). We acknowledge the use of clean-room facilities from the “Centrale de Proximité Paris-Centre” and Renatech network. This work was supported by French state funds managed by the Agence Nationale de la Recherche through the grants Bright (No. ANR-21-CE24-0012), MixDFerro (No. ANR-21-CE09-0029), Quicktera (No. ANR-22-CE09-0018), E-map (No. ANR-23-CE50-0025), DIRAC (No. ANR-24-ASM1-0001), camIR (No. ANR-24-CE42-2757), Piquant (No. ANR-24-CE09-0786), and NanoSaclay (No. ANR-10-LABX-0035).

## AUTHOR DECLARATIONS

### Conflict of Interest

The authors have no conflicts to disclose.

### Author Contributions

**Claire Abadie:** Conceptualization (equal); Investigation (equal); Methodology (equal); Writing – original draft (equal). **Nicolas Ledos:** Formal analysis (equal); Investigation (equal); Writing – original draft (equal). **Ye Mou:** Conceptualization (equal); Investigation (equal). **Mariarosa Cavallo:** Writing – review & editing (equal). **Erwan Bossavit:** Writing – review & editing (equal). **Huichen Zhang:** Writing – review & editing (equal). **Albin Colle:** Writing – review & editing (equal). **Tommaso Gemo:** Writing – review & editing (equal). **Adrien Khalili:** Writing – review & editing (equal). **Yoann Prado:** Data curation (equal); Resources (equal). **Bruno Gallas:** Investigation (equal); Resources (equal); Supervision (equal); Writing – review & editing (equal). **Grégory Vincent:** Supervision (equal); Writing – review & editing (equal). **Mathieu Mivelle:** Conceptualization (equal); Formal analysis (equal); Resources (equal); Writing – review & editing (equal). **Emmanuel Lhuillier:** Conceptualization (equal); Project administration (equal); Resources (equal); Writing – original draft (equal); Writing – review & editing (equal).

## DATA AVAILABILITY

The data that support the findings of this study are available within the article and its [supplementary material](#).

## REFERENCES

- <sup>1</sup>N. Ledos, T. H. Dang, M. Cavallo, H. Zhang, E. Bossavit, A. Khalili, L. N. Do, C. Gréboval, S. Ithurria, J. K. Utterback, D. Pierucci, G. Vincent, A. Vasanelli, and E. Lhuillier, "Stop blaming hopping conduction in nanocrystal arrays, use it for active photonics!" *Adv. Mater. Technol.* **9**(6), 2301463 (2024).
- <sup>2</sup>N. Yan, Y. Qiu, X. He, X. Tang, Q. Hao, and M. Chen, "Plasmonic enhanced nanocrystal infrared photodetectors," *Materials* **16**(8), 3216 (2023).
- <sup>3</sup>M. Chen, L. Shao, S. V. Kershaw, H. Yu, J. Wang, A. L. Rogach, and N. Zhao, "Photocurrent enhancement of HgTe quantum dot photodiodes by plasmonic gold nanorod structures," *ACS Nano* **8**(8), 8208–8216 (2014).
- <sup>4</sup>T. H. Dang, A. Vasanelli, Y. Todorov, C. Sirtori, Y. Prado, A. Chu, C. Gréboval, A. Khalili, H. Cruguel, C. Delerue, G. Vincent, and E. Lhuillier, "Bias tunable spectral response of nanocrystal array in a plasmonic cavity," *Nano Lett.* **21**(15), 6671–6677 (2021).
- <sup>5</sup>X. Tang, M. M. Ackerman, G. Shen, and P. Guyot-Sionnest, "Towards infrared electronic eyes: flexible colloidal quantum dot photovoltaic detectors enhanced by resonant cavity," *Small* **15**(12), 1804920 (2019).
- <sup>6</sup>T. H. Dang, M. Cavallo, A. Khalili, C. Dabard, E. Bossavit, H. Zhang, N. Ledos, Y. Prado, X. Lafosse, C. Abadie, D. Gacemi, S. Ithurria, G. Vincent, Y. Todorov, C. Sirtori, A. Vasanelli, and E. Lhuillier, "Multiresonant grating to replace transparent conductive oxide electrode for bias selected filtering of infrared photoresponse," *Nano Lett.* **23**(18), 8539–8546 (2023).
- <sup>7</sup>A. R. Dhawan, C. Belacel, J. U. Esparza-Villa, M. Nasilowski, Z. Wang, C. Schwob, J.-P. Hugonin, L. Coolen, B. Dubertret, P. Senellart, and A. Maitre, "Extreme multiexciton emission from deterministically assembled single-emitter subwavelength plasmonic patch antennas," *Light Sci. Appl.* **9**(1), 33 (2020).
- <sup>8</sup>C. Belacel, B. Habert, F. Bigourdan, F. Marquier, J.-P. Hugonin, S. Michaelis de Vasconcellos, X. Lafosse, L. Coolen, C. Schwob, C. Javaux, B. Dubertret, J.-J. Greffet, P. Senellart, and A. Maitre, "Controlling spontaneous emission with plasmonic optical patch antennas," *Nano Lett.* **13**(4), 1516–1521 (2013).
- <sup>9</sup>J. Roither, M. V. Kovalenko, S. Pichler, T. Schwarzl, and W. Heiss, "Nanocrystal-based microcavity light-emitting devices operating in the telecommunication wavelength range," *Appl. Phys. Lett.* **86**(24), 241104 (2005).
- <sup>10</sup>X. Tang, M. M. Ackerman, and P. Guyot-Sionnest, "Acquisition of hyperspectral data with colloidal quantum dots," *Laser Photonics Rev.* **13**(11), 1900165 (2019).
- <sup>11</sup>E. Bossavit, H. Zhang, N. Ledos, M. Cavallo, D. Mastrolito, L. Curti, A. Khalili, A. Colle, P. Lample, M. Weis, F. Margaillan, X. Lafosse, Y. Prado, E. Péronne, D. Pierucci, S. Ithurria, D. Boschetto, B. T. Diroll, A. Degiron, and E. Lhuillier, "Shaping infrared luminescence of colloidal nanocrystals using dielectric microcavity," *Adv. Funct. Mater.* **34**(39), 2403532 (2024).
- <sup>12</sup>Y. Yifat, M. Ackerman, and P. Guyot-Sionnest, "Mid-IR colloidal quantum dot detectors enhanced by optical nano-antennas," *Appl. Phys. Lett.* **110**(4), 041106 (2017).
- <sup>13</sup>A. Caillas and P. Guyot-Sionnest, "Uncooled high detectivity mid-infrared photoconductor using HgTe quantum dots and nanoantennas," *ACS Nano* **18**(12), 8952–8960 (2024).
- <sup>14</sup>K. A. Sergeeva, D. V. Pavlov, A. A. Seredin, E. V. Mitsai, A. A. Sergeev, E. B. Modin, A. V. Sokolova, T. C. Lau, K. V. Baryshnikova, M. I. Petrov, S. V. Kershaw, A. A. Kuchmizhak, K. S. Wong, and A. L. Rogach, "Laser-printed plasmonic metasurface supporting bound states in the continuum enhances and shapes infrared spontaneous emission of coupled HgTe quantum dots," *Adv. Funct. Mater.* **33**(44), 2307660 (2023).
- <sup>15</sup>T. H. Dang, C. Abadie, A. Chu, M. Cavallo, A. Khalili, C. Dabard, E. Bossavit, H. Zhang, Y. Prado, D. Pierucci, J. K. Utterback, Y. Todorov, C. Sirtori, J. Jaeck, G. Vincent, A. Vasanelli, B. Fix, and E. Lhuillier, "Bias reconfigurable photoresponse of an infrared nanocrystal film integrated into a coupled Fabry-Perot resonator," *ACS Photonics* **10**(5), 1601–1607 (2023).
- <sup>16</sup>C. Abadie, L. Paggi, A. Fabas, A. Khalili, T. H. Dang, C. Dabard, M. Cavallo, R. Alchaar, H. Zhang, Y. Prado, N. Bardou, C. Dupuis, X. Z. Xu, S. Ithurria, D. Pierucci, J. K. Utterback, B. Fix, G. Vincent, P. Bouchon, and E. Lhuillier, "Helmholtz resonator applied to nanocrystal-based infrared sensing," *Nano Lett.* **22**(21), 8779–8785 (2022).
- <sup>17</sup>A. Caillas, S. Suffit, P. Filloux, E. Lhuillier, and A. Degiron, "Anomalous absorption in arrays of metallic nanoparticles: A powerful tool for quantum dot optoelectronics," *Nano Lett.* **22**(5), 2155–2160 (2022).
- <sup>18</sup>E. Bailly, J.-P. Hugonin, J.-R. Coudeville, C. Dabard, S. Ithurria, B. Vest, and J.-J. Greffet, "2D silver-nanoplatelets metasurface for bright directional photoluminescence, designed with the local Kirchhoff's law," *ACS Nano* **18**(6), 4903–4910 (2024).
- <sup>19</sup>J.-J. Greffet, P. Bouchon, G. Brucoli, and F. Marquier, "Light emission by non-equilibrium bodies: Local Kirchhoff law," *Phys. Rev. X* **8**(2), 021008 (2018).
- <sup>20</sup>P. He, A. Caillas, G. Bouliard, I. Hamdi, P. Filloux, M. Ravaro, E. Lhuillier, and A. Degiron, "Observation of quasi-invariant photocarrier lifetimes in PbS nanocrystal assemblies coupled to resonant and nonresonant arrays of optical antennas," *ACS Photonics* **11**(2), 437–444 (2024).
- <sup>21</sup>E. Bossavit, T. H. Dang, P. He, M. Cavallo, A. Khalili, C. Dabard, H. Zhang, D. Gacemi, M. G. Silly, C. Abadie, B. Gallas, D. Pierucci, Y. Todorov, C. Sirtori, B. T. Diroll, A. Degiron, E. Lhuillier, and A. Vasanelli, "Plasmon-assisted directional infrared photoluminescence of HgTe nanocrystals," *Adv. Opt. Mater.* **11**(22), 2300863 (2023).
- <sup>22</sup>T. H. Dang, A. Khalili, C. Abadie, C. Gréboval, M. Cavallo, H. Zhang, E. Bossavit, J. K. Utterback, E. Dandeu, Y. Prado, G. Vincent, S. Ithurria, Y. Todorov, C. Sirtori, A. Vasanelli, and E. Lhuillier, "Nanocrystal-based active photonics device through spatial design of light-matter coupling," *ACS Photonics* **9**(7), 2528–2535 (2022).
- <sup>23</sup>X. Tang, M. M. Ackerman, and P. Guyot-Sionnest, "Thermal imaging with plasmon resonance enhanced HgTe colloidal quantum dot photovoltaic devices," *ACS Nano* **12**(7), 7362–7370 (2018).
- <sup>24</sup>T. H. Dang, C. Abadie, A. Khalili, C. Gréboval, H. Zhang, Y. Prado, X. Z. Xu, D. Gacemi, A. Descamps-Mandine, S. Ithurria, Y. Todorov, C. Sirtori, A. Vasanelli, and E. Lhuillier, "Broadband enhancement of mid-wave infrared absorption in a multi-resonant nanocrystal-based device," *Adv. Opt. Mater.* **10**(9), 2200297 (2022).
- <sup>25</sup>T. Simon, X. Li, J. Martin, D. Khlopin, O. Stéphan, M. Kociak, and D. Gérard, "Aluminum Cayley trees as scalable, broadband, multiresonant optical antennas," *Proc. Natl. Acad. Sci. U. S. A.* **119**(4), e2116833119 (2022).
- <sup>26</sup>H.-L. Chen, A. Cattoni, R. De Lépinay, A. W. Walker, O. Höhn, D. Lackner, G. Siefert, M. Faustini, N. Vandamme, J. Goffard, B. Behaghel, C. Dupuis, N. Bardou, F. Dimroth, and S. Collin, "A 19.9%-efficient ultrathin solar cell based on a 205-nm-thick GaAs absorber and a silver nanostructured back mirror," *Nat. Energy* **4**(9), 761–767 (2019).
- <sup>27</sup>H. Zhang, R. Alchaar, Y. Prado, A. Khalili, C. Gréboval, M. Cavallo, E. Bossavit, C. Dabard, T. H. Dang, C. Abadie, C. Methivier, D. Darson, V. Parahyba, P. Potet, J. Ramade, M. G. Silly, J. K. Utterback, D. Pierucci, S. Ithurria, and E. Lhuillier, "Material perspective on HgTe nanocrystal-based short-wave infrared focal plane arrays," *Chem. Mater.* **34**(24), 10964–10972 (2022).
- <sup>28</sup>S. S. Wang and R. Magnusson, "Theory and applications of guided-mode resonance filters," *Appl. Opt.* **32**(14), 2606–2613 (1993).
- <sup>29</sup>A. Khalili, M. Weis, S. G. Mizrahi, A. Chu, T. H. Dang, C. Abadie, C. Gréboval, C. Dabard, Y. Prado, X. Z. Xu, E. Péronne, C. Livache, S. Ithurria, G. Patriarche, J. Ramade, G. Vincent, D. Boschetto, and E. Lhuillier, "Guided-mode resonator coupled with nanocrystal intraband absorption," *ACS Photonics* **9**(3), 985–993 (2022).
- <sup>30</sup>C. Gréboval, A. Chu, D. V. Magalhaes, J. Ramade, J. Qu, P. Rastogi, A. Khalili, S.-S. Chee, H. Aubin, G. Vincent, S. Bals, C. Delerue, and E. Lhuillier, "Ferroelectric gating of narrow band-gap nanocrystal arrays with enhanced light-matter coupling," *ACS Photonics* **8**(1), 259–268 (2021).
- <sup>31</sup>P. Rastogi, A. Chu, T. H. Dang, Y. Prado, C. Gréboval, J. Qu, C. Dabard, A. Khalili, E. Dandeu, B. Fix, X. Z. Xu, S. Ithurria, G. Vincent, B. Gallas, and E. Lhuillier, "Complex optical index of HgTe nanocrystal infrared thin films and its use for short wave infrared photodiode design," *Adv. Opt. Mater.* **9**(10), 2002066 (2021).
- <sup>32</sup>A. Chu, C. Gréboval, N. Goubet, B. Martinez, C. Livache, J. Qu, P. Rastogi, F. A. Bresciani, Y. Prado, S. Suffit, S. Ithurria, G. Vincent, and E. Lhuillier, "Near unity absorption in nanocrystal based short wave infrared photodetectors using guided mode resonators," *ACS Photonics* **6**(10), 2553–2561 (2019).

- <sup>33</sup>S. Keuleyan, E. Lhuillier, and P. Guyot-Sionnest, "Synthesis of colloidal HgTe quantum dots for narrow mid-IR emission and detection," *J. Am. Chem. Soc.* **133**(41), 16422–16424 (2011).
- <sup>34</sup>T. H. Dang, M. Cavallo, A. Khalili, E. Bossavit, H. Zhang, Y. Prado, C. Abadie, E. Dandeu, S. Ithurria, G. Vincent, Y. Todorov, C. Sirtori, A. Vasanelli, and E. Lhuillier, "Designing rules for an efficient metallic mid-infrared transparent electrode dedicated to nanocrystal-based devices," *ACS Photonics* **11**(5), 1928–1934 (2024).
- <sup>35</sup>Y. Luo, S. Zhang, X. Tang, and M. Chen, "Resonant cavity-enhanced colloidal quantum-dot dual-band infrared photodetectors," *J. Mater. Chem. C* **10**(21), 8218–8225 (2022).
- <sup>36</sup>P. Rastogi, E. Izquierdo, C. Gréboval, M. Cavallo, A. Chu, T. H. Dang, A. Khalili, C. Abadie, R. Alchaar, S. Pierini, H. Cruguel, N. Witkowski, J. K. Utterback, T. Brule, X. Z. Xu, P. Hollander, A. Ouerghi, B. Gallas, M. G. Silly, and E. Lhuillier, "Extended short-wave photodiode based on CdSe/HgTe/Ag<sub>2</sub>Te stack with high internal efficiency," *J. Phys. Chem. C* **126**(32), 13720–13728 (2022).
- <sup>37</sup>C. Gréboval, E. Izquierdo, C. Abadie, A. Khalili, M. Cavallo, A. Chu, T. H. Dang, H. Zhang, X. Lafosse, M. Rosticher, X. Z. Xu, A. Descamps-Mandine, A. Ouerghi, M. G. Silly, S. Ithurria, and E. Lhuillier, "HgTe nanocrystal-based photodiode for extended short-wave infrared sensing with optimized electron extraction and injection," *ACS Appl. Nano Mater.* **5**(6), 8602–8611 (2022).
- <sup>38</sup>J. Yang, Y. Lv, Z. He, B. Wang, S. Chen, F. Xiao, H. Hu, M. Yu, H. Liu, X. Lan, H.-Y. Hsu, H. Song, and J. Tang, "Bi<sub>2</sub>S<sub>3</sub> electron transport layer incorporation for high-performance heterostructure HgTe colloidal quantum dot infrared photodetectors," *ACS Photonics* **10**(7), 2226–2233 (2023).
- <sup>39</sup>M. M. Ackerman, M. Chen, and P. Guyot-Sionnest, "HgTe colloidal quantum dot photodiodes for extended short-wave infrared detection," *Appl. Phys. Lett.* **116**(8), 083502 (2020).

**Genetic Algorithm Driven Optimization of Guided Mode Resonator Coupled to Infrared Nanocrystals Film**

Claire Abadie<sup>1</sup>, Nicolas Ledos<sup>1</sup>, Ye Mou<sup>1</sup>, Mariarosa Cavallo<sup>1</sup>, Erwan Bossavit<sup>1</sup>, Huichen Zhang<sup>1</sup>, Albin Colle<sup>1</sup>, Tommaso Gemo<sup>1</sup>, Adrien Khalili<sup>1</sup>, Yoann Prado<sup>1</sup>, Bruno Gallas<sup>1</sup>, Gregory Vincent<sup>2</sup>, Mathieu Mivelle<sup>1</sup>, Emmanuel Lhuillier<sup>1\*</sup>

<sup>1</sup> Sorbonne Université, CNRS, Institut des NanoSciences de Paris, 4 place Jussieu, 75005 Paris, France.

<sup>2</sup> DOTA, ONERA, Université Paris Saclay, 6 Chemin de la Vauve aux Granges, 91120 Palaiseau, France.

\*To whom correspondence should be sent [el@insp.upmc.fr](mailto:el@insp.upmc.fr)

## Table of content

1. Nanocrystals growth .....	2
2. Input for electromagnetic simulation .....	2
3. Structure optimized through genetic algorithm .....	4
4. Device fabrication and characterization .....	8
5. Simulation for periodic structure .....	11
6. REFERENCES .....	11



## 1. Nanocrystals growth

**Chemicals:** Mercury chloride ( $\text{HgCl}_2$ , Sigma-Aldrich, 99%), mercury bromide ( $\text{HgBr}_2$ , Alfa Aesar), tellurium powder (Te, Sigma-Aldrich, 99.99%), trioctylphosphine (TOP, Alfa, 90%), oleylamine (OLA, Acros, 80-90%), dodecanethiol (DDT, Sigma-Aldrich, 98%), 2-mercaptoethanol (MPOH, Merck, >99%), and N,N-dimethylformamide (DMF, VWR), toluene (VWR, 99.8%) were used. All chemicals were used without further purification, except oleylamine that is centrifuged before use. **Mercury compounds are highly toxic. Handle them with special care.**

**1 M TOP:Te precursor:** Te powder (6.35 g) was mixed in 50 mL of TOP in a 100 mL three-neck flask. The flask was kept under vacuum at room temperature for 5 mins, then the temperature was raised to 100 °C. Next, degassing of the flask was conducted for the next 20 mins. The atmosphere was switched to nitrogen, and the temperature was raised to 275 °C. The solution was stirred until a clear orange color was obtained. The flask was cooled to room temperature, and the color changed to yellow. Finally, this solution was transferred to a nitrogen-filled glove box for storage.

**HgTe NCs growth:** In a 100 mL three neck flask, 540 mg of  $\text{HgCl}_2$  and 50 mL of oleylamine were degassed under vacuum at 110°C for 30 min. Then, the atmosphere was switched to  $\text{N}_2$  and the temperature stabilized at 82°C. Meanwhile 2 mL of TOP:Te (1M) were extracted from glove box and mixed with 8 mL of oleylamine. Then, the TOP:Te solution was quickly injected. After 3 min, 10 mL of a mixture of 10% DDT in toluene were injected and a water bath was used to decrease quickly the temperature. The content of the flask was splitted over 3 centrifuge tubes and MeOH was added. After centrifugation the formed pellet was redispersed in 1 centrifuge tube with toluene. The solution was precipitated a second time with absolute EtOH. Again, the formed pellet was redispersed in toluene. Finally, the nanocrystals were centrifuged in pure toluene to get rids of the lamellar phase. The solid phase was discarded and the dispersion filtered (cut off 0.22 $\mu\text{m}$ ).

## 2. Input for electromagnetic simulation

For FDTD simulations, we use the following input for the complex optical index. The dielectric constant of the gold is taken equal to  $\varepsilon(E) = 1 - \frac{2.29 \times 10^7}{E(E + i130)}$  With E is the photo energy in meV<sup>1</sup>. The number  $2.29 \times 10^7$  represents plasma frequency while 130 represents metal loss n and k of Au can be calculated from:  $n = \frac{1}{2}((\varepsilon'^2 + \varepsilon''^2) + \varepsilon')^{\frac{1}{2}}$  and  $k = \frac{1}{2}((\varepsilon'^2 + \varepsilon''^2) - \varepsilon')^{\frac{1}{2}}$

$\varepsilon'$  and  $\varepsilon''$  are real and imaginary part of the dielectric function.

For the complex optical index of the HgTe NC film, we use values from references<sup>2,3</sup> and illustrated in **Figure S 1**.

For the silica layer used as optical spacer between the back reflector and the grating we use  $n=1.45$  (without frequency dependence) and  $k=0$ , which means assuming glass is transparent below 2.5  $\mu\text{m}$ .

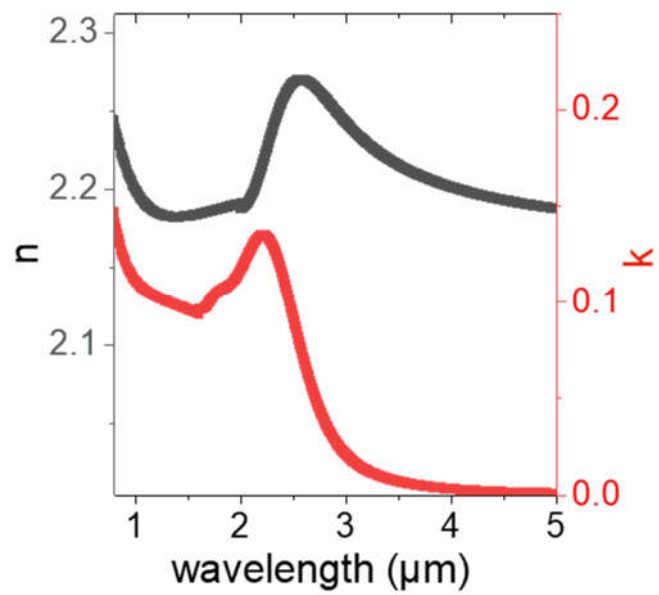


**Figure S 1** Complex optical index of HgTe.

### 3. Structure optimized through genetic algorithm

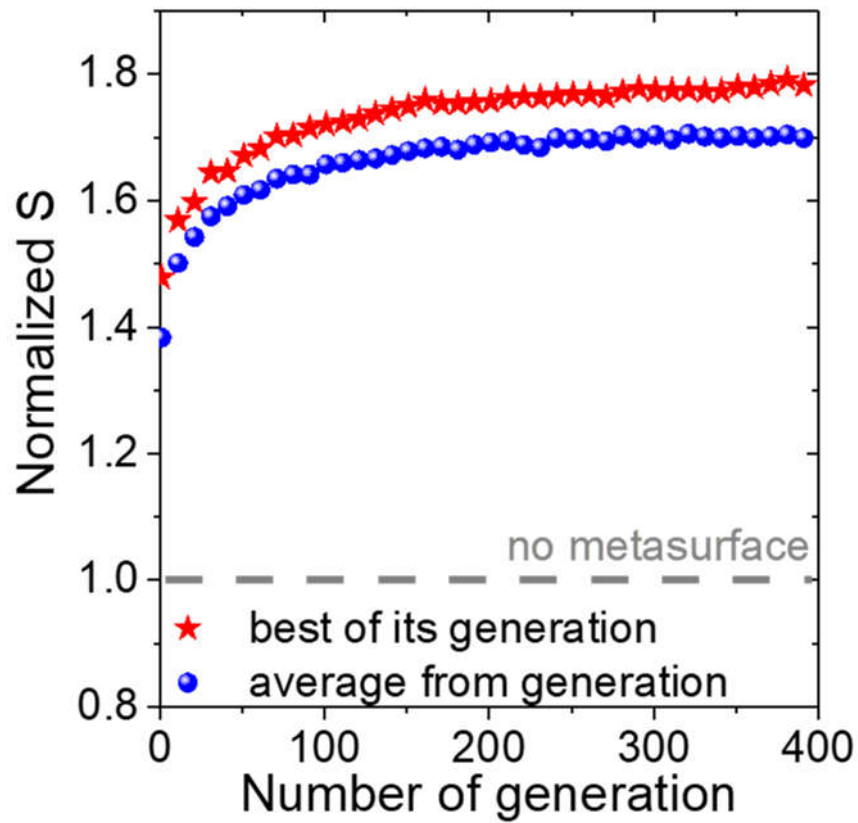


**Figure S 2** Normalized  $S$  value as a function of the number of generations during the GA optimization procedure. In blue the average value for the normalized  $S$  among the generation and in red the highest  $S$  value from the generation

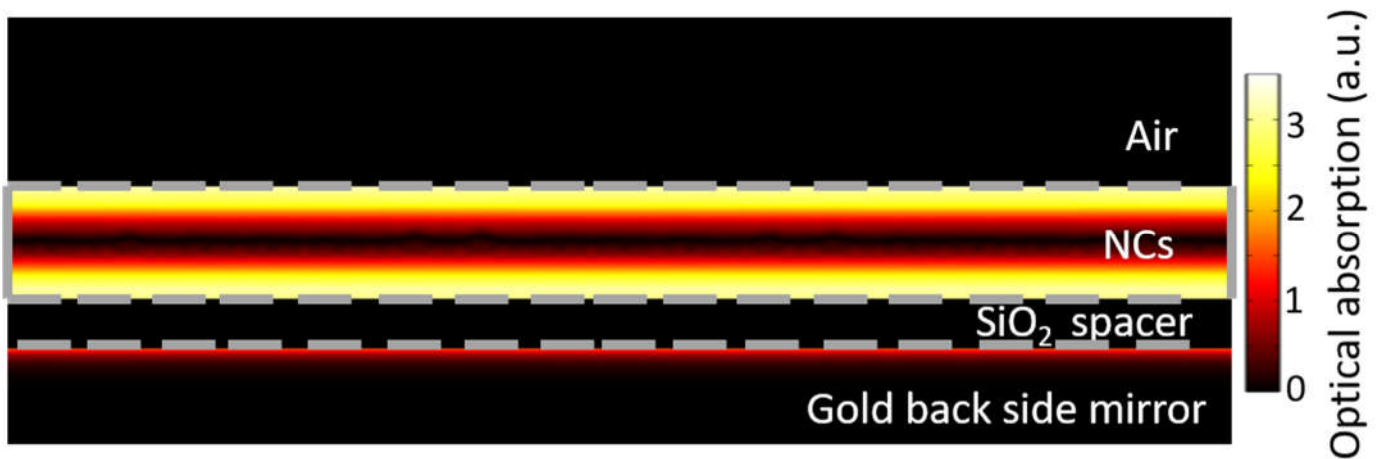


**Figure S 3** Absorption map at 1.2  $\mu\text{m}$  for the structure without metasurface.

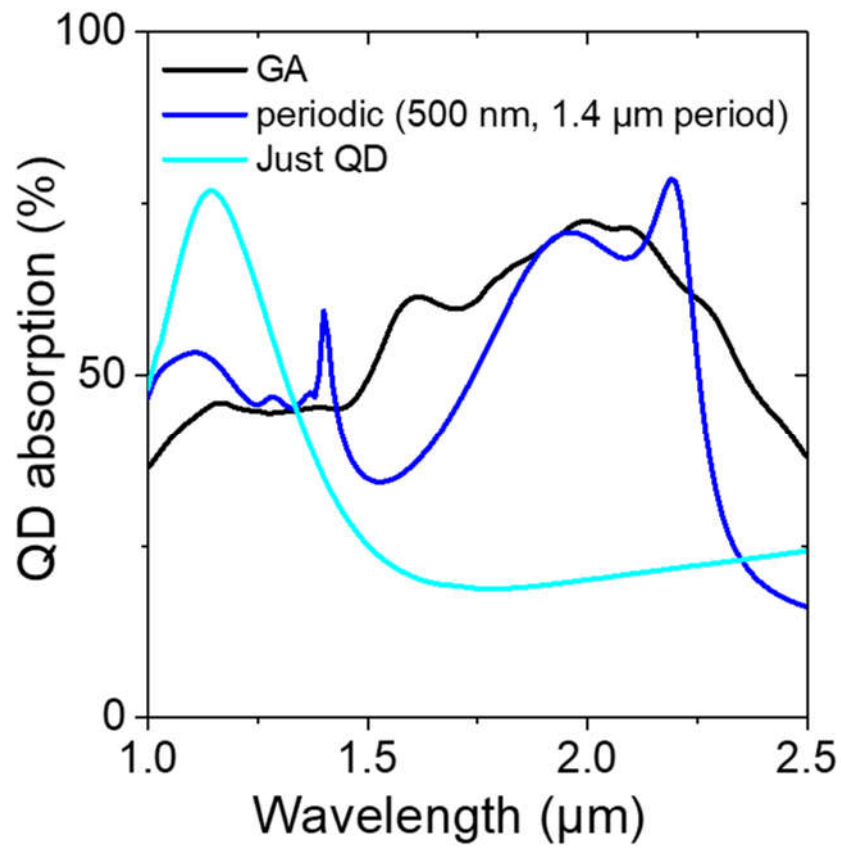


**Figure S 4 Benefit from GA design.** Simulated absorption spectra for the pristine NC film, a periodic GMR (500 nm digit with 1.4  $\mu\text{m}$  period) and for the film coupled to the optimized GA structure in TM polarization.



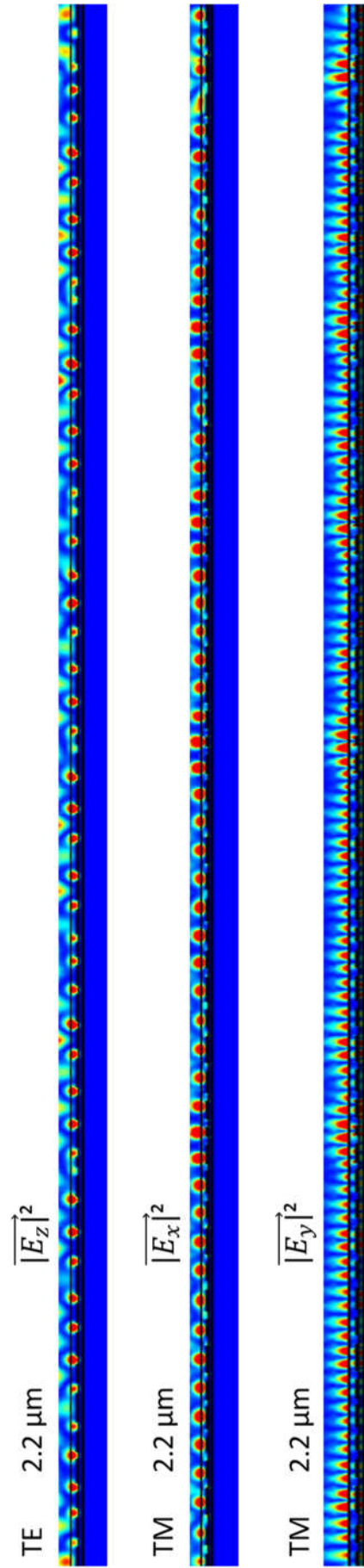


**Figure S 5 Electric field maps at the band edge.** top.  $|\vec{E}_z|^2$  in TE polarization. middle.  $|\vec{E}_x|^2$  in TM polarization and bottom  $|\vec{E}_y|^2$  in TM polarization.

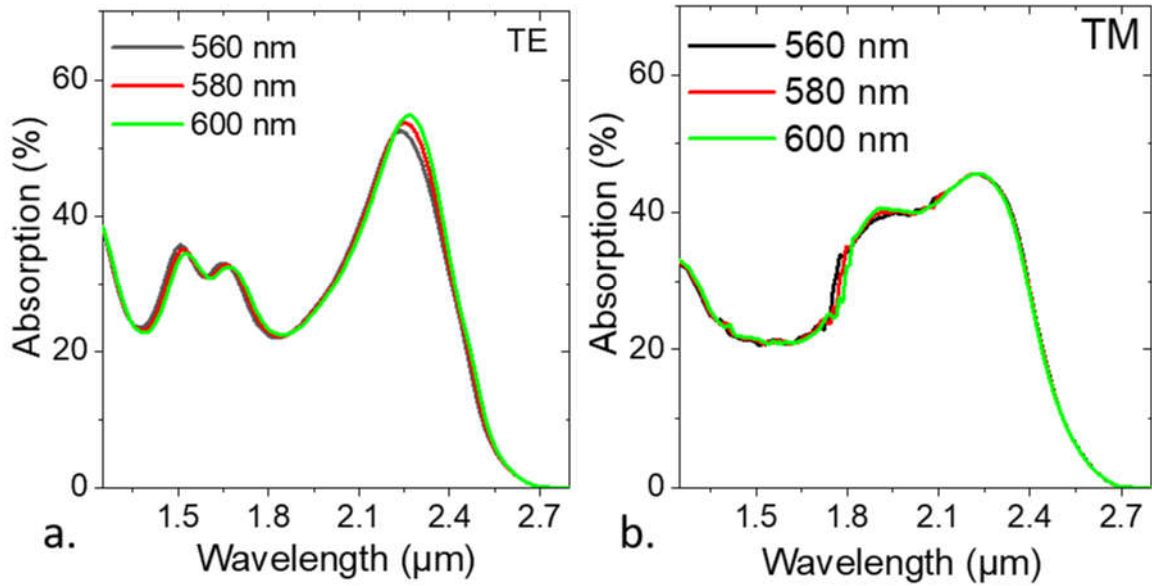


**Figure S 6 a. (resp b.) Absorption spectra of the GMR GA FFT structure in TE (resp TM) polarization as the value of  $O_i$  parameter is tuned from the average value (580 nm) to close values.**

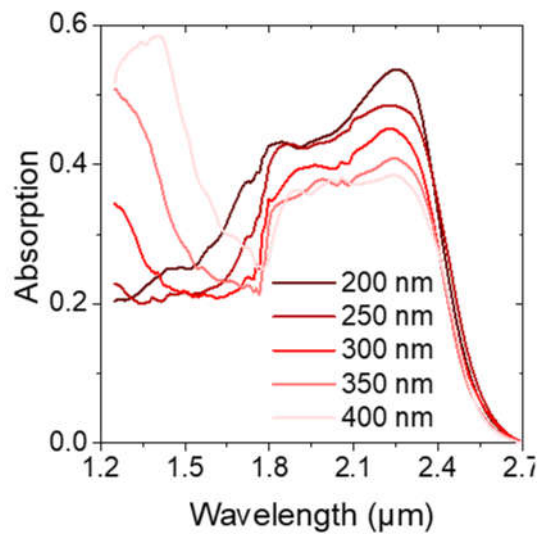


**Figure S 7 Absorption spectra in TM polarization for various thicknesses of the film.**

#### 4. Device fabrication and characterization

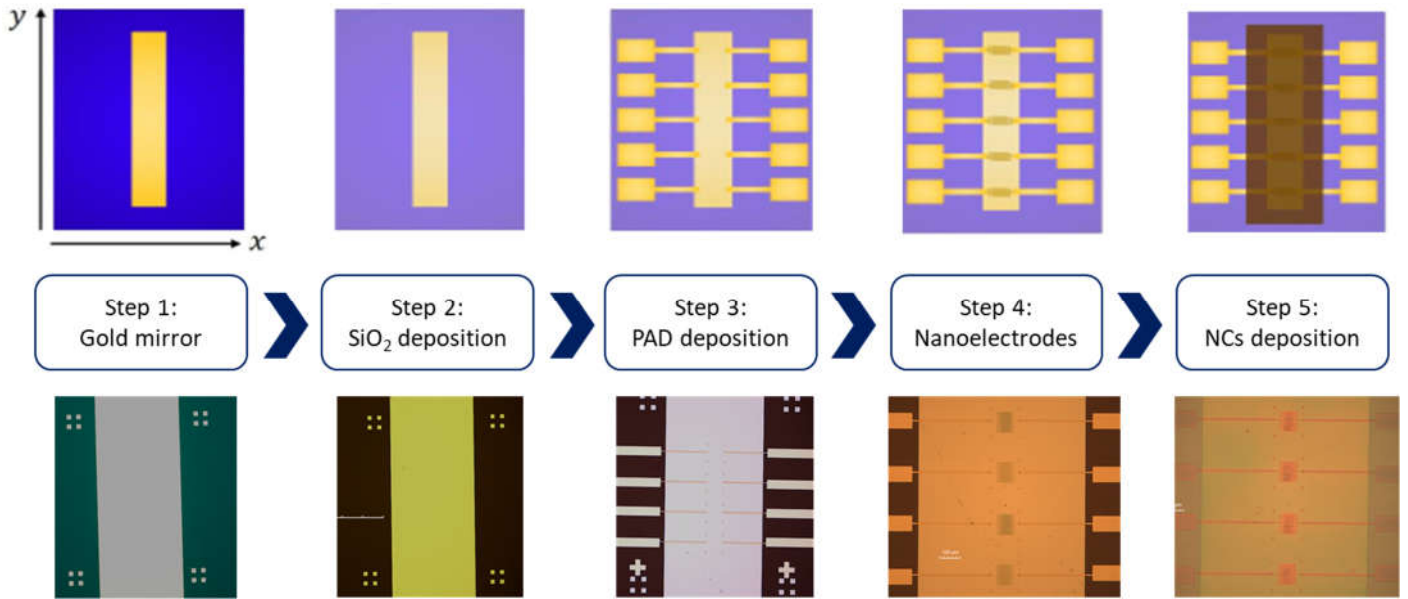


**Figure S 8 Schematic (top) and microscopy image (bottom) of each step of the fabrication.**

**Step 1: Deposition of the gold mirror:** The surface of Si/SiO<sub>2</sub> wafer (400 nm oxide layer) is cleaned by sonication in acetone. The wafer is rinsed with acetone, then isopropanol and dried with a N<sub>2</sub> gun. A final cleaning is made using an O<sub>2</sub> plasma. An adhesion promoter (TI PRIME) is spin-coated onto the substrate and baked at 120 °C for 2 min. AZ5214E is spin-coated and baked at 110 °C for 90 s. The substrate is exposed under UV through a pattern mask for 1.5 s. The film is then baked at 125 °C for 2 min in order to invert the resist. Then a 40 s flood exposure is performed. The resist is developed using a bath of AZ726 for 35 s, rinsed in pure water and finally dried with N<sub>2</sub>. We then deposit 5 nm of titanium and 80 nm of gold using thermal evaporation. The lift-off is performed by dipping the film in acetone for 1 hour. The gold mirror is rinsed using isopropanol and dried with a N<sub>2</sub> flow.

**Step 2: Insulating gold mirror:** The deposition of the SiO<sub>2</sub> layer was performed using a Corial D250 PECVD system. The substrates were placed in the deposition chamber and the temperature was set at 280°C. Once the plasma generated the substrates were exposed to an atmosphere of SiH<sub>4</sub> and N<sub>2</sub>O for 193 seconds in order to obtain a 120 nm thick film.

**Step 3: Deposition of macroscopic pads for reporting electric contacts:** After having rinsed the sample with acetone and isopropanol, the adhesion promoter and the resist are deposited as described in step 1. The sample is then exposed through a second chromium mask for 1.5 s. The same resist inversion process as described in step 1 (annealing + flood exposure) is performed before developing the sample in AZ726 developer for 35 s and rinsing it in pure water. The patterned sample is then introduced into a VINCI evaporator for deposition of 5 nm of Titanium and 150 nm of gold. At the end, the sample is dipped in acetone overnight to remove remaining resist.

**Step 4: Deposition of nanoelectrodes by e-beam lithography:** After having rinsed the sample with acetone and isopropanol, a layer of A6 PMMA 950 is spin-coated onto the substrate and baked for 3 min at 180 °C. The samples are transferred in a Zeiss Supra 40 SEM with Raith elphy quantum device for electron beam lithography. The operating bias is set to 20 kV and the aperture to 10 µm. The current is measured at 20 pA. The dose is set at 150 µC.cm<sup>-2</sup>. The PMMA is developed by dipping the film in a solution of MIBK:isopropanol (1:3) for 50 s, rinsed in pure isopropanol for 50 s and finally dried with N<sub>2</sub>. We then deposit a 5 nm layer of titanium and an 80 nm layer of gold using thermal evaporation. The lift-off is performed by dipping the film in hot acetone (40°C) overnight.

**Step 5: HgTe NCs deposition: HgTe ink:** 1.5 mL of the HgTe solution in toluene (1.2 OD at 400 nm after a 1000x dilution) is mixed with 1.5 mL of exchange solution (15 mg HgCl<sub>2</sub>, 9 mL DMF, 1 mL MPOH) and 1mL of DMF. The solution is stirred throughout vortex and sonication for 3 min to help the ligand exchange. Then, the solution is washed 2 times using hexane (4 mL of hexane is added and the solution, after vortexing the hexane is discarded). Then, the solution is precipitated by adding toluene and centrifuged at 6000 rpm for 4 min. The supernatant is discarded and the QDs are dried using a N<sub>2</sub> gun. Finally, the NCs are redispersed in 275 µL of DMF, centrifuged for 1 min at 6000 rpm and filtered through a 0.22 µm PTFE filter.

**Step 6: Film deposition:** The nanoelectrodes are plasma-cleaned for 5 min. Then 35 µL of the ink are deposited on the substrate. The spin-coating steps are 750 rpm (acceleration 750 rpm.s<sup>-1</sup>) for 120 s and 2000 rpm (750 rpm.s<sup>-1</sup>) for 45 s. The obtained film thickness is about 300 nm.

**Photocurrent spectra:** The device is enclosed in a closed-cycle cryostat and cooled down to the desired temperature. The head of the cryostat is brought in the sample compartment of a Fischer iS50 FTIR spectrometer and illumination is provided by the focused Globar source through two ZnSe windows (one on the outer cryostat enclosure and one on the cold shield). The photocurrent is amplified using a Femto DLPCA-200 transimpedance amplifier, which also serves as a bias source. The output of the amplifier is sent back to the FTIR spectrometer through the *ad hoc* external detector adapter. All spectra are normalized to the background spectrum, acquired with a flat-response DTGS detector in the same spectral range to account for source and optical path spectra.

**Activation energy:** Devices are mounted on the cold finger of a closed-cycle cryostat equipped with a cold shield. The samples are cooled down to 200 K, and current flow is measured with a Keithley 2634b source-meter which is also used to bias the sample. The temperature is measured with a Lakeshore 325 temperature controller using a calibrated sensor on the sample holder. Resulting  $I(T)$  curves are fitted to an Arrhenius model  $I_0 = Ae^{-Ea/kT}$  between 300 K and 200 K, allowing for the extraction of the activation energy  $Ea$ .

**Responsivity measurement:** The source is a blackbody Omega BB-4A at 980 °C placed 45 cm away from the sample. The diameter of the blackbody is 1 inch. The current from the device is amplified using a Femto DLPCA-200 to bias the sample and then fed into a Zurich Instruments MFLI Lock-in amplifier. A germanium 1.8 µm high pass filter is utilized to suppress the high energy part of the blackbody spectrum. The total power is calculated according to the formula:  $P = A_D \cdot \pi \cdot \cos(\beta) \cdot \sin^2(\alpha) \cdot \int_{\lambda_{min}}^{\lambda_{max}} \frac{hc^2}{\lambda^5} \cdot \frac{1}{e^{hc/\lambda kT}} d\lambda$  where  $\alpha$  is the solid angle illuminated,  $\beta$  is the angle of the sample (0° corresponds to sample perpendicular to the light illumination),  $A_D$  is the device area,  $h$  is the Planck constant,  $c$  the light velocity,  $k$  is the Boltzmann constant and  $T$  the temperature. The



light is chopped at 100 Hz with an optical chopper. The photocurrent is measured with the oscilloscope under varying applied biases. The sample is mounted on the cold finger of a closed cycle cryostat.

**Noise measurement.** The current from the device (at different biases, kept in the dark) is amplified by a Femto DLPCA-200, then fed into a Stanford research systems model SR780 spectrum analyzer. The sample is mounted on the cold finger of a closed cycle cryostat.

**Time response measurements:** In order to probe the time response, the device is excited with a ns pulsed laser MPL-H-1573 with a wavelength of 1573 nm and a power of 0.05 W. The pulses are 1.15 ns long and have a repetition rate of 100 Hz. The current from the device (mounted on the cold finger of a closed cycle cryostat) is amplified by a Femto DHPCA-100, also used to bias the device. The photocurrent is measured with the Rohde&Schwarz RTE 1102 oscilloscope. The signal from the laser is also diverted into a Thorlabs InGaAs detector. This signal from the InGaAs detector is fed into the same oscilloscope in order to trigger the signal from the device. The time response is defined as the fit of an exponential decay close to the pulse.

## 5. Simulation for periodic structure

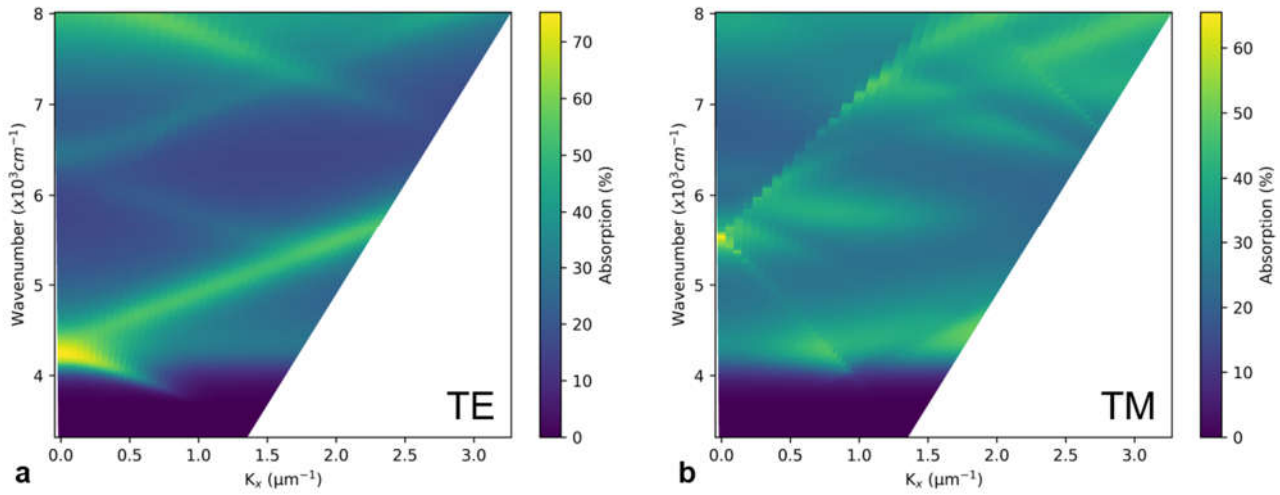


**Figure S 9 Dispersion maps for the periodic structure.** *a. (resp b.) Dispersion map in TE (resp TM) polarization for the periodic GMR structure.*

## 6. REFERENCES

- <sup>1</sup> T.H. Dang, C. Abadie, A. Khalili, C. Gréboval, H. Zhang, Y. Prado, X.Z. Xu, D. Gacemi, A. Descamps-Mandine, S. Ithurria, Y. Todorov, C. Sirtori, A. Vasanelli, and E. Lhuillier, “Broadband Enhancement of Mid-Wave Infrared Absorption in a Multi-Resonant Nanocrystal-Based Device,” *Adv. Opt. Mater.* **10**(9), 2200297 (2022).
- <sup>2</sup> B. Chehaibou, C. Abadie, Y. Prado, X.Z. Xu, G. Vincent, B. Gallas, G. Mugny, A. Arnaud, E. Lhuillier, and C. Delerue, “Modeling HgTe Complex Optical Index from Bulk to Nanocrystal Layers,” *J. Phys. Chem. C* **127**(28), 13789–13799 (2023).
- <sup>3</sup> P. Rastogi, A. Chu, T.H. Dang, Y. Prado, C. Gréboval, J. Qu, C. Dabard, A. Khalili, E. Dandeu, B. Fix, X.Z. Xu, S. Ithurria, G. Vincent, B. Gallas, and E. Lhuillier, “Complex Optical Index of HgTe Nanocrystal Infrared Thin Films and Its Use for Short Wave Infrared Photodiode Design,” *Adv. Opt. Mater.* **9**(10), 2002066 (2021).